Transmission resonances and zeros in multiband models

R. Chris Bowen, William R. Frensley, and Gerhard Klimeck
Eric Jonsson School of Engineering and Computer Science, University of Texas at Dallas, Richardson, Texas 75083-0688

Roger K. Lake
Central Research Laboratories, Texas Instruments Incorporated, Dallas, Texas 75265
(Received 20 March 1995)

We report on an efficient numerical technique for directly locating transmission resonances and zeros in semiconductor heterostructures using tight-binding multiband models. The quantum transmitting boundary method is employed to generate the inverse of the retarded Green's function $G^R(E)$ in the tight-binding representation. The poles of $G^R(E)$ are located by solving a nonlinear non-Hermitian eigenvalue problem. The eigenvalues are calculated using a shift and invert nonsymmetric Lanczos algorithm followed by Newton refinement. We demonstrate that resonance line shapes are accurately characterized by the location of the poles and zeros of $G^R(E)$ in the complex energy plane. The real part of the pole energy corresponds to the resonance peak and the imaginary part corresponds to the resonance width. A Fano resonance is characterized by a zero-pole pair in the complex energy plane. In the case of an isolated Fano resonance, the zero always occurs on the real energy axis. However, we demonstrate that for overlapping Fano resonances the zeros can move off of the real axis in complex conjugate pairs. This behavior is examined using a simple analytic model for multichannel scattering.

I. INTRODUCTION

For several years now it has been recognized that the single-band effective-mass model is insufficient to simulate quantum transport in material systems that are currently under investigation. This has prompted a growing effort on the part of theorists to include realistic band structures in quantum transport simulations.[1–5] Many of the interesting effects in quantum heterostructure devices are described by the transmission resonances obtained when these devices are coupled to semi-infinite reservoirs. In this work we describe an efficient numerical technique for directly locating transmission resonances and zeros in quantum devices using realistic band-structure models.

We choose to model semiconductor band structures using localized basis tight-binding models. The quantum transmitting boundary method (QTBM) is employed to couple the tight-binding Hamiltonian to semi-infinite reservoirs. The resulting operator is the inverse of the retarded Green's function $G^R(E)$ in the tight-binding representation. The transmission resonances and zeros of the device correspond to the poles and zeros of $G^R(E)$. The evaluation of the poles of $G^R(E)$ requires the solution of a nonlinear eigenvalue problem. We have developed a shift and invert nonsymmetric Lanczos algorithm, that quickly provides accurate initial guesses to the eigenvalues which are of interest. These eigenvalues are then refined using Newton's method.

The location of the poles and zeros of $G^R(E)$ provide significant information concerning the physics of quantum devices. Resonance line shapes are accurately characterized by the location of the poles and zeros of $G^R(E)$. This is demonstrated by fitting a partial fraction expansion to a resonance line shape utilizing the pole and zero locations. In addition, the location of the poles and zeros of $G^R(E)$ provides insight into the phenomenon of Fano resonances in quantum devices. We have found that Fano resonances due to Γ-X tunneling in indirect gap barriers may or may not exhibit transmission zeros. We shall show that in the case of overlapping Fano resonances, the zeros of the Green's function move off of the real energy axis in conjugate pairs. Thus, the transmission probability does not vanish between the resonances. A quantitative explanation of this phenomenon is provided using a simple analytic model for Fano resonances.

Section II will present the QTBM for localized basis tight-binding Hamiltonians. The numerical technique for locating the poles and zeros of $G^R(E)$ will be detailed in Sec. III. In Sec. IV, we shall demonstrate this numerical technique by calculating poles and zeros for a GaAs/AlAs/GaAs heterostructure using the $sp3s^*$ tight-binding basis. The general behavior of the poles and zeros in indirect gap barriers is analyzed in Sec. V using a simple analytic model. In Sec. VI, band-structure effects on Fano resonance linewidths are investigated and in Sec. VII, we shall demonstrate accurate line-shape fitting using the poles and zeros of $G^R(E)$.

II. QTBM FOR TIGHT-BINDING MODELS

We shall describe band structure using nearest-neighbor tight-binding Hamiltonians. In this section we shall not be concerned with the details of these Hamiltonians. The basis set is assumed to be spatially localized and only nearest-neighbor coupling is considered. The

0163-1829/95/52(4)/2754(12)/$06.00

Schrödinger equation in such a representation may be expressed as

$$(H\Psi)_j = -S_j^\dagger \Psi_{j-1} + D_j \Psi_j - S_{j+1}\Psi_{j+1} = E\Psi_j \ , \quad (1)$$

where Ψ_j is a subvector containing the localized basis coefficients corresponding to the jth spatial node. The Hamiltonian matrix elements are contained in the submatrices S_j and D_j. We shall define the points $j = 1$ and $j = n$ as the limits of the domain, which define the mesoscopic device as shown in Fig. 1. To calculate scattering states, we must couple this Hamiltonian to semi-infinite regions on either side of the device. This is accomplished by generating a unitary matrix, which relates the amplitudes of the Bloch states in the contact regions with the localized basis coefficients at the device boundaries. In order to generate this matrix, we must first calculate the Bloch states that exist in the semi-infinite contacting regions. Assuming that both the transverse basis and the spatial potential do not vary in the contacting regions, we may invoke the Bloch theorem to calculate these states:

$$\sum_{k'} \Big[z_{1;m}^{-1} S_{1;kk'}^\dagger + (IE - D)_{1;kk'} + z_{1;m} S_{1;kk'} \Big] \chi_{1;k'm} = 0. \quad (2)$$

$$\sum_{k'} \Big[z_{n;m}^{-1} S_{n;kk'}^\dagger + (IE - D)_{n;kk'} + z_{n;m} S_{n;kk'} \Big] \chi_{n;k'm} = 0. \quad (3)$$

Here $z_{1;m}$ ($z_{n;m}$) is the discrete spatial propagation factor for the mth Bloch state in the left (right) contact region. χ_1 (χ_n) is a matrix whose mth column contains the localized basis coefficients for the mth Bloch state in the left (right) contact region. These equations define a generalized eigenvalue problem, which can be readily solved if S^{-1} exists: (treatment of models for which S is singular is discussed in Appendix A)[7]

$$\begin{bmatrix} 0 & 1 \\ S_1^{-1}S_1^\dagger & -S_1^{-1}D_1 \end{bmatrix} \begin{bmatrix} \chi_{1;m} \\ z_{1;m}\chi_{1;m} \end{bmatrix} = z_{1;m} \begin{bmatrix} \chi_{1;m} \\ z_{1;m}\chi_{1;m} \end{bmatrix} . \quad (4)$$

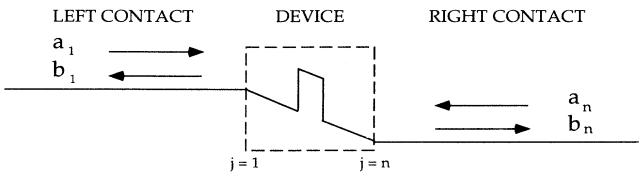

FIG. 1. Graphical illustration of a device coupled to semi-infinite contact regions. The solid line represents the conduction band edge, and a and b are subvectors containing incoming and outgoing Bloch state amplitudes, respectively. The QTBM expresses the continuum quantum states of the system in terms of the incoming amplitudes a_1 and a_n.

The solution of this eigenvalue problem results in $2N$ states where N is the number of transverse basis states. Time reversal symmetry dictates that half of these states propagate or decay to the right while the other half propagate or decay to the left. For convenience, these states are sorted according to their direction of propagation and stored in the matrices χ_1^R and χ_1^L, respectively.

The general solution to Schrödinger's equation for a given energy E in the semi-infinite contact regions may be expressed as follows:

$$\Psi_j = \sum_m \Big[a_{1;m} z_{1;m}^{j-1} \chi_{1;km}^R + b_{1;m} z_{1;m}^{1-j} \chi_{1;km}^L \Big] \quad \text{for } j \le 1 \ , \quad (5)$$

$$\Psi_j = \sum_m \Big[a_{n;m} z_{n;m}^{n-j} \chi_{n;km}^L + b_{n;m} z_{n;m}^{j-n} \chi_{n;km}^R \Big] \quad \text{for } j \ge n \ . \quad (6)$$

As illustrated in Fig. 1, $a_{1;m}$ ($a_{n;m}$) is the amplitude of the incoming component of the mth state in the left (right) contacting region and $b_{1;m}$ ($b_{n;m}$) is the amplitude of the outgoing component. The wave function in the device is coupled to the contact regions by invoking this solution at the device boundaries:

$$\begin{bmatrix} \Psi_0 \\ \Psi_1 \end{bmatrix} = \begin{bmatrix} \chi_1^R Z_1^{-1} & \chi_1^L Z_1 \\ \chi_1^R & \chi_1^L \end{bmatrix} \begin{bmatrix} a_1 \\ b_1 \end{bmatrix} , \quad (7)$$

$$\begin{bmatrix} \Psi_{n+1} \\ \Psi_n \end{bmatrix} = \begin{bmatrix} \chi_n^L Z_n^{-1} & \chi_n^R Z_n \\ \chi_n^L & \chi_n^R \end{bmatrix} \begin{bmatrix} a_n \\ b_n \end{bmatrix} , \quad (8)$$

where Z is a diagonal matrix containing the discrete propagation factors ($Z_{1;mm'} = z_{1;m}\delta_{mm'}$) between spatial nodes. The matrices in Eqs. (7) and (8) provide the relationships required to construct the open system boundary conditions. To obtain the final QTBM equations, we express the wave-function subvectors at the device boundaries in terms of the incoming Bloch state amplitude vectors a_1 and a_n. Defining

$$\begin{bmatrix} \alpha_1 & \beta_1 \\ \gamma_1 & \delta_1 \end{bmatrix} = \begin{bmatrix} \chi_1^R Z_1^{-1} & \chi_1^L Z_1 \\ \chi_1^R & \chi_1^L \end{bmatrix}^{-1} , \quad (9)$$

$$\begin{bmatrix} \alpha_n & \beta_n \\ \gamma_n & \delta_n \end{bmatrix} = \begin{bmatrix} \chi_n^L Z_n^{-1} & \chi_n^R Z_n \\ \chi_n^L & \chi_n^R \end{bmatrix}^{-1} , \quad (10)$$

we obtain

$$a_1 = \alpha_1 \Psi_0 + \beta_1 \Psi_1 \ , \quad (11)$$

$$a_n = \alpha_n \Psi_{n+1} + \beta_n \Psi_n \ . \quad (12)$$

These equations are inserted into the matrix representation of the tight-binding Schrödinger equation resulting in the following block-tridiagonal system:[6]

$$\begin{bmatrix} \alpha_1(E) & \beta_1(E) & & & & \\ S_1^\dagger & E-D_1 & S_2 & & & \\ & S_2^\dagger & E-D_2 & S_3 & & \\ & & \ddots & \ddots & \ddots & \\ & & & S_n^\dagger & E-D_n & S_{n+1} \\ & & & & \beta_n(E) & \alpha_n(E) \end{bmatrix} \begin{bmatrix} \Psi_0 \\ \Psi_1 \\ \Psi_2 \\ \vdots \\ \Psi_n \\ \Psi_{n+1} \end{bmatrix} = \begin{bmatrix} a_1 \\ 0 \\ 0 \\ \vdots \\ 0 \\ a_n \end{bmatrix} . \tag{13}$$

The incoming Bloch amplitudes are set by the values contained in the vectors a_1 and a_n. The solution of this equation produces the appropriate scattering state for the mesoscopic structure described by the tight-binding Hamiltonian. We have chosen to construct our Hamiltonian operator such that a_1 and a_n are in the Bloch basis. Transforming the QTBM equations into the tight-binding basis results in an operator that is Hermitian everywhere except the corner diagonal blocks. In this basis, the open system boundary conditions may be represented by a self-energy, which is added to the corner diagonal blocks of the closed system Hamiltonian (see Appendix B).

III. LOCATION OF THE POLES AND ZEROS OF THE GREEN'S FUNCTION

Since the inhomogeneous terms in Eq. (13) represent incoming state amplitudes, the matrix operator (which we shall denote as $E - H_{\mathrm{QTBM}}$) in this equation is the inverse of the retarded Green's function in the localized basis representation:

$$E - H_{\mathrm{QTBM}}(E) = \left[G^R(E)\right]^{-1} . \tag{14}$$

The location of the poles and zeros of $G^R(E)$ characterize the transmission line shapes in the vicinity of transmission resonances and zeros. We therefore seek an efficient method for locating the poles and zeros of $G^R(E)$ in the complex energy plane. The poles of $G^R(E)$ correspond to the eigenvalues of the $H_{\mathrm{QTBM}}(E)$. However, since the boundary condition submatrices (α_1, β_1, α_n, and β_n) are energy dependent, the eigenvalue problem is nonlinear. To solve this problem we first generate $H_{\mathrm{QTBM}}(E)$ at a trial energy (E_T) and calculate its eigenvalues. These eigenvalues are then used as initial guesses to iteratively locate the zeros of the determinant of $E - H_{\mathrm{QTBM}}(E)$.

To obtain the initial guesses, we must calculate the eigenvalues of a non-Hermitian block-tridiagonal matrix. Though sparse, this matrix is quite large ($N \approx 3000$ for a 100-nm device) when realistic band-structure models are employed. The standard matrix diagonalization routines for non-Hermitian matrices do not preserve the block-tridiagonal sparseness of our matrix; therefore, they are computationally prohibitive. Initially, a left-right (LR) algorithm, which preserves the block-tridiagonal form, was employed to solve this problem. However, it was soon realized that complete diagonalization of this matrix is too computationally intensive and another approach was necessary. We are only interested in eigenvalues corresponding to states that are involved in carrier transport. In almost all cases, these states are contained within a small portion of the total eigenspectrum of $H_{\mathrm{QTBM}}(E)$. In order to efficiently calculate these eigenvalues, we have developed a shift and invert nonsymmetric (SINS) Lanczos algorithm. This algorithm computes a subspace that accurately represents the region of the eigenspectrum which is of interest.

The nonsymmetric Lanczos algorithm generates a tridiagonal matrix T, which is similar to the original general matrix A:[8]

$$X^{-1}AX = T = \begin{bmatrix} \epsilon_1 & \gamma_1 & & \\ \eta_1 & \epsilon_2 & \ddots & \\ & \ddots & \ddots & \gamma_{n-1} \\ & & \eta_{n-1} & \epsilon_n \end{bmatrix} , \tag{15}$$

$$X = [x_1, ..., x_n] , \tag{16}$$

$$X^{-T} = Y = [y_1, ..., y_n] . \tag{17}$$

The Lanczos recursion that generates the tridiagonal basis is written as follows.

$$\beta_j x_{j+1} = Ax_j - \epsilon_j x_j - \gamma_{j-1} x_{j-1} , \tag{18}$$

$$\gamma_j y_{j+1} = A^T y_j - \epsilon_j y_j - \eta_{j-1} y_{j-1} . \tag{19}$$

However, the similarity transformation of a nonsymmetric matrix to tridiagonal form using this algorithm is not stable.[7] Our algorithm makes use of the fact that long before the Lanczos tridiagonalization is complete, the extremal eigenvalues of T_j (T after j Lanczos recursions) are very good approximations to the extremal eigenvalues of A.[8] Therefore, we shift A to the portion of the eigenvalue spectrum that is of interest and perform the Lanczos recursion on the inverse of the shifted matrix.[9] The extremal eigenvalues of the shifted and inverted matrix correspond to the eigenvalues of the original matrix in the vicinity of the shift:

$$A\psi_i = E_i \psi_i , \tag{20}$$

$$(A - sI)^{-1} \psi_i' = E_i' \psi_i' , \tag{21}$$

$$E_i = E_i'^{-1} + s . \tag{22}$$

The shift and invert nonsymmetric Lanczos recursion is written as follows:

$$\beta_j x_{j+1} = (A - sI)^{-1} x_j - \epsilon_j x_j - \gamma_{j-1} x_{j-1} , \tag{23}$$

$$\gamma_j y_{j+1} = (A - sI)^{-T} y_j - \epsilon_j y_j - \eta_{j-1} y_{j-1} . \tag{24}$$

The inverted matrices are not stored explicitly. We lower-

TABLE I. Eigenvalue comparison between the block-tridiagonal LR and SINL algorithms. The test matrix $H_{\mathrm{QTBM}}(E_T)$ was generated using the $sp3s^*$ Hamiltonian (block dimension = 10). The dimension of the test matrix is 110.

Block-tridiagonal LR	SINL	Relative error
1.670 499 849 086 829 7 $-i1.924\,854\,874\,620\,785\,9 \times 10^{-5}$	1.670 499 849 086 775 3 $-i1.924\,854\,871\,793\,598\,0 \times 10^{-5}$	3.3×10^{-14}
1.674 789 213 627 013 1 $-i2.132\,329\,131\,194\,187\,5 \times 10^{-3}$	1.674 789 213 627 048 1 $-i2.132\,329\,131\,140\,281\,9 \times 10^{-3}$	2.1×10^{-14}
1.822 213 534 091 728 5 $-i4.984\,816\,491\,529\,066\,1 \times 10^{-3}$	1.822 213 534 091 807 1 $-i4.984\,816\,491\,592\,372\,3 \times 10^{-3}$	4.3×10^{-14}

upper (LU) decompose the shifted matrix and perform two back substitutions at each iteration. The recursion is halted when the order T_j is some fraction of the order of A. We have found that generating more than approximately 50 Lanczos vectors does not provide significant new information in the subspace. Thus, in the case of large matrices, the order of the subspace is only a very small fraction of the order of the original matrix. The eigenvalues of T_j are computed using a partial shift LR algorithm and transformed using Eq. (22).[10] In the neighborhood of s, we find very good agreement between these transformed eigenvalues and the actual eigenvalues of A. A comparison between eigenvalues calculated using the SINS Lanczos algorithm and the block-tridiagonal LR algorithm is shown in Table I. The SINS Lanczos algorithm requires only one LU decomposition of A and $2j$ back substitutions while the LR algorithm requires approximately $2N$ (where N = order of A) similarity transformations. The execution times of the two algorithms are compared in Table II. We have found that the eigenvalues of $H_{\mathrm{QTBM}}(E_T)$ obtained with the SINS Lanczos algorithm are good approximations to the eigenvalues of $H_{\mathrm{QTBM}}(E)$. In order to refine these eigenvalues, Newton's method is used to locate the zeros of the determinant of $E - H_{\mathrm{QTBM}}(E)$. Convergence is generally achieved in 3 – 6 iterations.

The model of multiple states per longitudinal site is isomorphic to a one-band electron waveguide model with multiple lateral sites per longitudinal site. Just as the multiple lateral sites allow multiple current paths through position space, which can destructively interfere in an electron waveguide, the multiple states allow multiple current paths through state space, which can destructively interfere in the multiband model. The energies for which the channels destructively interfere result in zeros of $G^R(E)$. The zeros of $G^R(E)$ are found using Newton's method to locate the zeros of the outgoing amplitudes corresponding to propagating states. We start the Newton iteration on the real energy axis on either side of each pole of $G^R(E)$. The wave functions at these energies are calculated by directly solving Eq. (13). In subsequent iterations, iterative methods are used to solve this system of equations. Convergence is generally achieved in 10 – 15 iterations.

Our method for locating the poles and zeros of $G^R(E)$ may be summarized as follows.

(i) Divide the energy domain (real part) of interest into segments of $\approx$0.1 eV.

(ii) Calculate eigenvalues of $H_{\mathrm{QTBM}}(E_T)$ in each of these segments using the SINS Lanczos algorithm. E_T is chosen to be located in the center of each segment.

(iii) Refine these eigenvalues by using Newton's method to determine energies for which $\det|E - H_{\mathrm{QTBM}}(E)| = 0$. These energies correspond to the poles of $G^R(E)$.

(iv) Locate the zeros of $G^R(E)$ using Newton's method to locate the zeros of the outgoing propagating state amplitudes.

TABLE II. Execution time comparison between the block-tridiagonal LR and SINL algorithms. The test matrix $H_{\mathrm{QTBM}}(E_T)$ was generated using the $sp3s^*$ Hamiltonian (block dimension = 10). Eigenvalues were located in an energy range of 0.5 eV using four values of E_T separated by 0.1 eV within this range. For a matrix of this size, the eigenvalues calculated with the SINL algorithm are actually more accurate than those calculated with the LR algorithm. This is most likely due to accumulated roundoff error in the LR algorithm. The comparison was executed on a Sun Sparc 10 workstation.

N	Block-tridiagonal LR	SINL	Execution time ratio
1100	5.7 CPU hours	3.6 CPU minutes	95

IV. FANO RESONANCES IN INDIRECT GAP BARRIERS

To demonstrate the use of these techniques on a mesoscopic structure, we shall investigate tunneling in single-barrier GaAs/AlAs/GaAs heterostructures. For several years now it has been recognized that the single-band effective-mass model is insufficient to accurately describe tunneling through indirect gap barriers such as AlAs.[2,5,11] The interaction between quasibound X states in the barrier with continuum Γ states results in resonance-antiresonance features known as Fano resonances.[13] Such features have been observed experimentally as negative differential resistance in GaAs/AlAs/GaAs single-barrier heterostructures.[12] In order to describe tunneling in these structures, one must use models that describe material band structures accurately throughout the Brillouin zone. In this work

we choose to describe band structure using the ten-band $sp3s^*$ tight-binding model.[14] The $sp3s^*$ model employs five atomiclike orbitals to describe the electronic band structure of semiconductors. We are modeling zinc-blende structure crystals that contain two atoms per unit cell giving a total of ten transverse basis states. The $sp3s^*$ tight-binding parameters used for the following calculation are those published in Ref. 5.

The transmission coefficient as a function of incident electron energy is shown in Fig. 2 for a GaAs/AlAs/GaAs single barrier. Both ten-band (solid line) and single-band (dashed line) calculations are displayed. The poles and zeros of $G^R(E)$ (ten-band model) for this structure are plotted below the transmission curve. The Γ- and X-valley energy band profiles for this structure are illustrated in Fig. 3. The AlAs barrier is five unit cells (14 Å) thick and the incoming electron is propagating in the Γ valley with transverse momentum equal to zero. The most striking difference between the different band-structure models are the resonance-antiresonance features predicted by the ten-band model. The resonance-antiresonance line shapes are due to resonances of the type described by Fano.[13] The Fano line shape is characterized by a pole-zero pair in the complex energy plane.[15] The real part of the pole is associated with the location of the transmission resonance and the imaginary part of the pole determines the spectral width of the resonance. The zero, which is located on the real energy axis, determines the energy for which the transmission probability vanishes. Fano resonances occur whenever a bound state is coupled to a set of continuum states.[13] Since the profile of the X point conduction band minimum forms a quantum well (as shown in Fig. 3), bound states with X-like symmetry exist in the barrier. In addition to the bound X states, there also exists a set of continuum evanescent Γ states in the barrier. The coupling of the continuum Γ and bound X states results in Fano resonances in AlAs barriers.

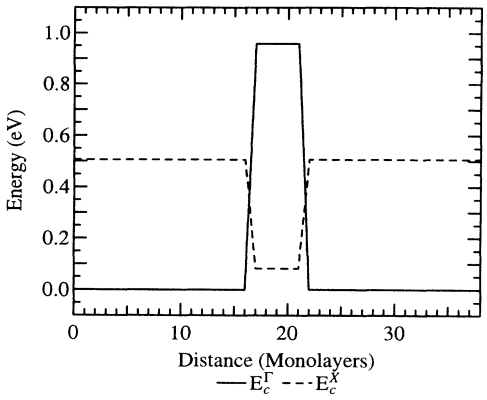

FIG. 3. Conduction band profile for 14-Å GaAs/AlAs/GaAs single-barrier heterostructure. Solid line, conduction band edge at Γ; dashed line, conduction band edge at X.

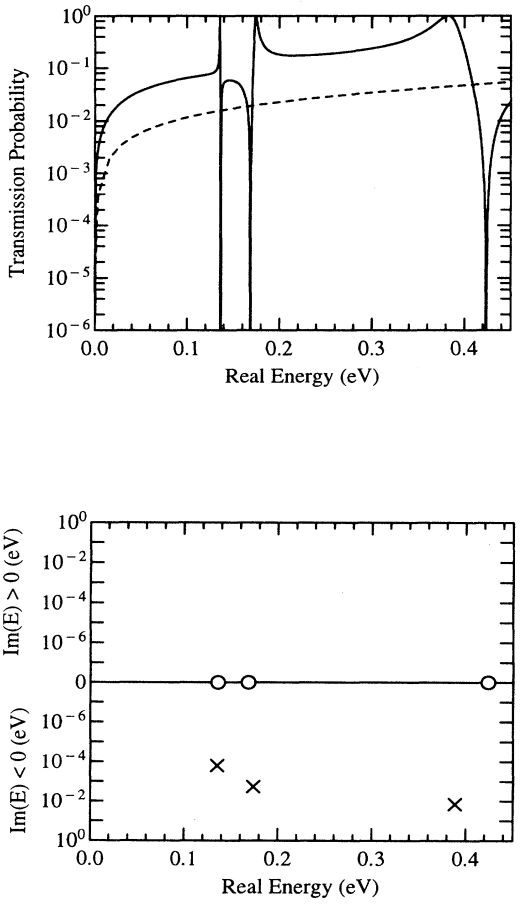

FIG. 2. (Top) Transmission coefficient vs incident electron energy for a 14-Å AlAs barrier (no applied potential). Solid line, ten-band model; dashed line, one-band model. (Bottom) Location of the poles (crosses) and zeros (circles) of $G^R(E)$ for this structure. Energy is referenced from the GaAs Γ-valley minimum in both figures.

The resonance-antiresonance line shape may be understood qualitatively by considering the nature of the parallel conduction channels as illustrated in Fig. 4. An incident electron can tunnel through the barrier by tunneling from the Γ state in the emitter through the quasibound X state in the barrier and back to the Γ state in the collector. We label this channel Γ-X-Γ according to its symmetry in each region of the structure. The incident electron can also directly tunnel through the evanescent Γ state in the barrier. We label this channel Γ-Γ-Γ. The resonance is due to resonant tunneling through the quasibound X state. The antiresonance is due to destructive interference between the Γ-X-Γ channel and the Γ-Γ-Γ channel. As the energy of the incoming electron passes through a resonance, the Γ-X-Γ channel undergoes a phase shift of π. Thus, the Γ-Γ-Γ channel is out of phase with the Γ-X-Γ channel by a factor of π at energies below (or above) the resonance. The zero occurs when the magnitudes of the out of phase channels are equal.

The transmission coefficient as a function of incident electron energy for a 34-Å AlAs barrier is shown in Fig.

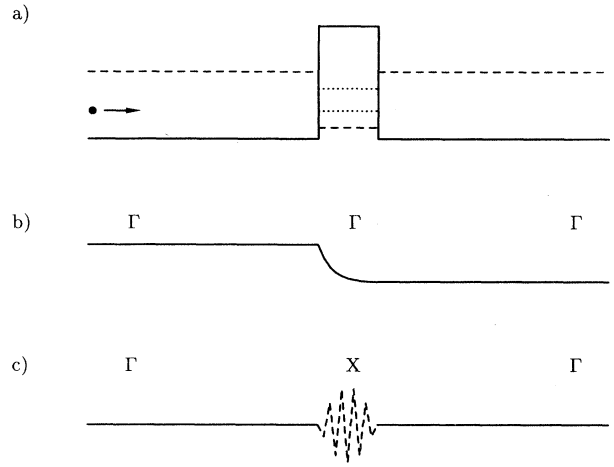

FIG. 4. (a) Band profile for indirect gap barrier. The solid line is the conduction band edge in the center of the Brillouin zone (Γ point). The dashed line is the conduction band edge at the edge of the Brillouin zone (X point). Dotted lines indicate energies of bound states confined by the X-point band profile. (b) Representation of the conduction channel with Γ symmetry throughout the structure. The phase shift of this channel varies slowly as a function of energy. (c) Representation of the conduction channel with X symmetry in the barrier. The excitation of an X bound state is illustrated. The phase shift of this channel undergoes a phase shift of π as the incident electron energy passes through a bound x state.

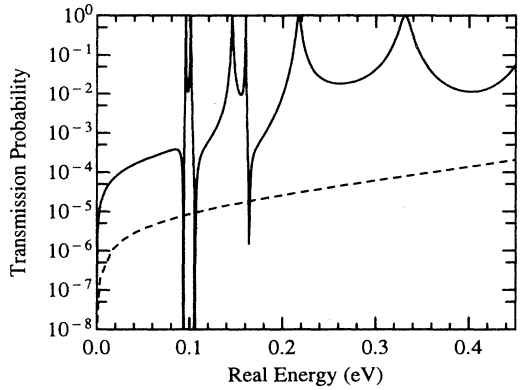

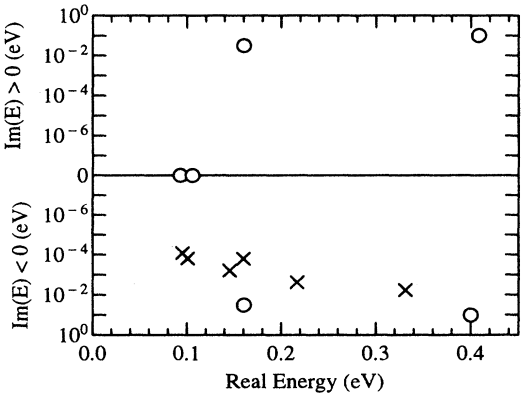

FIG. 5. (Top) Transmission coefficient vs incident electron energy for a 34-Å AlAs barrier (no applied potential). Solid line, ten-band model; dashed line, one-band model. (Bottom) Location of the poles (crosses) and zeros (circles) of $G^R(E)$ for this structure.

5. In this case, it is immediately apparent that there are resonances that are not accompanied by an antiresonance. This phenomenon has been reported by numerous workers and has been attributed to the hypothesis that conduction through the continuum Γ channel vanishes in wide barriers.[2] Under this hypothesis, the Green's function should not exhibit zeros and Fano resonances would vanish in wide barriers. However, the pole-zero plot in Fig. 5 clearly shows that all of the poles of $G^R(E)$ for the 34-Å barrier are accompanied by a zero and thus are indeed Fano resonances. Transmission zeros occur whenever the zero is located on the real energy axis. Transmission zeros vanish whenever the zero is not located on the real energy axis. We have found that when two Fano resonances overlap, the zeros associated with each resonance move off of the real energy axis in conjugate pairs. Therefore, in the case of overlapping Fano resonances, the transmission coefficient does not vanish.

V. BEHAVIOR OF THE POLES AND ZEROS IN INDIRECT GAP BARRIERS

In order to explain the behavior of the poles and zeros for overlapping Fano resonances, we shall employ a simple tight-binding model, which can be solved analytically. This model is schematically illustrated in Fig. 6. Each node in Fig. 6 represents a basis state in the model. B_1 and B_2 represent energies of the lowest and first excited bound X states, which are coupled to the continuum Γ states by the matrix elements V_1^L, V_1^R, V_2^L, and V_2^R. Transmission through the continuum Γ channel is represented by the hopping element t. After the inclusion of open system boundary conditions, the Hamiltonian for this model takes the following form:

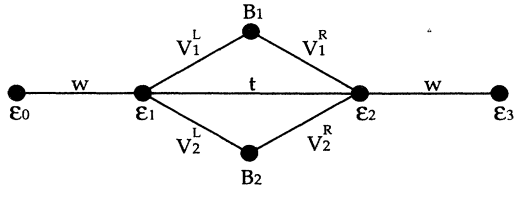

FIG. 6. Fano resonance model for one continuum and two bound states.

$$H - E = \begin{bmatrix} wz_L^{-1} & V_1^L & V_2^L & t \\ V_1^L & B_1 - E & 0 & V_1^R \\ V_2^L & 0 & B_2 - E & V_2^R \\ t & V_1^R & V_1^R & wz_R^{-1} \end{bmatrix} . \quad (25)$$

Here, $z_L = e^{ik_L a}$ and $z_R = e^{ik_R a}$ where k_L and k_R are the wave vectors in the left and right contact regions, and a is the distance between spatial nodes. The zeros of the Green's function for this model are given by the following expression:

$$E_{\text{zero}} = \frac{1}{2}[B_1 + B_2 + U_1 + U_2 \pm \sqrt{(B_2 + U_2 - B_1 - U_1)^2 + 4U_1U_2}] . \quad (26)$$

Here $U_1 = \frac{V_1^L V_1^R}{t}$ and $U_2 = \frac{V_2^L V_2^R}{t}$ are related to the zero energy shift relative to the bound state for each Fano resonance. Examination of Eq. (26) reveals that the zeros of $G^R(E)$ move off of the real axis under the following condition:

$$(B_2 + U_2 - B_1 - U_1)^2 + 4U_1U_2 < 0 . \quad (27)$$

Assuming $B_2 > B_1$, the necessary and sufficient criteria for Eq. (27) to hold are as follows:

$$U_1 > 0, \qquad U_2 < 0 , \quad (28)$$
$$B_2 - B_1 < |U_1| + |U_2| + 2\sqrt{|U_1||U_2|} .$$

As illustrated in Fig. 7, the relative sign of the matrix elements coupling the bound state to the left and right continuum channel is determined by the parity of the bound state. Therefore, $U_1 > 0$ implies that the state labeled B_1 is an even parity state while $U_2 < 0$ implies that B_2 is an odd parity state. The second criterion indicates that the zeros move off of the real axis when two states possessing this parity characteristic lie close together in energy. We would like to point out here that in the stub resonator structures simulated in Ref. 15, the matrix elements coupling the bound state to the continuum all have the same sign. This explains the fact that all of the zeros in stub resonator structures occur on the real axis.

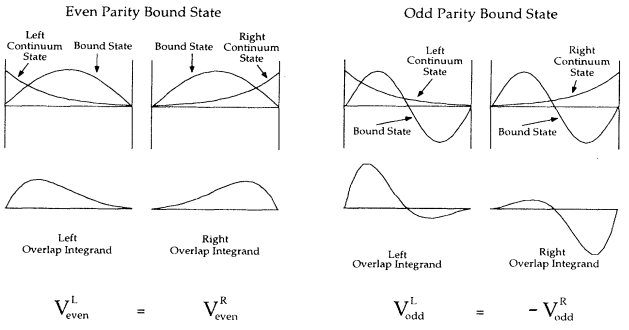

FIG. 7. Graphical illustration of the overlap matrix elements that couple a bound state to the continuum in an indirect gap barrier. (Left) The matrix elements that couple an even parity bound state to the left and right side of the barrier have the same sign. (Right) The matrix elements that couple an odd parity bound state to the left and right side of the barrier have opposite signs.

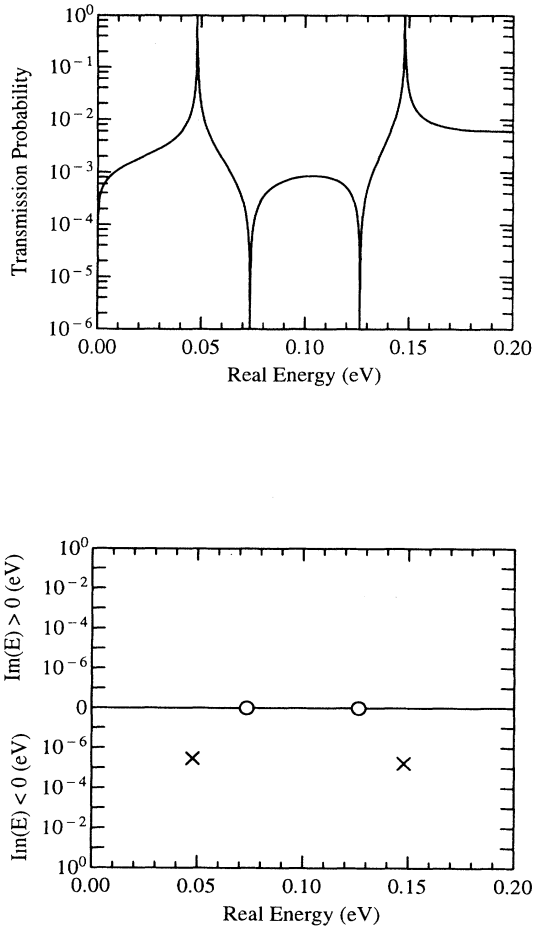

FIG. 8. (Top) Transmission coefficient vs incident electron energy for the analytic Fano resonance model (case 1). The matrix elements used are provided in Table III. In this case, the Fano resonances do not overlap and transmission zeros exist between the resonances. (Bottom) Location of the poles (crosses) and zeros (circles) of $G^R(E)$ for this Hamiltonian. Both zeros occur on the real axis.

We may illustrate the behavior of the poles and zeros associated with overlapping Fano resonances by analyzing a simple example. In Figs. 8 and 9, the transmission probability as a function of incident electron energy is shown for the analytic Fano resonance model. The poles and zeros of $G^R(E)$ for each case are plotted below the transmission curves. The values of the matrix elements used for each of these cases are provided in Table III. The signs of the matrix elements coupling the bound states to the continuum are chosen such that the lower energy state is of even parity and the higher energy state is of odd parity. In our example $|U_1| = |U_2| = 0.018$ eV, this implies that the zeros will move off the real axis for $B_2 - B_1 < 0.072$ eV. In Fig. 8, the difference between the bound state energies is 0.100 eV. In this case, the zeros lie on the real axis and the transmission probability van-

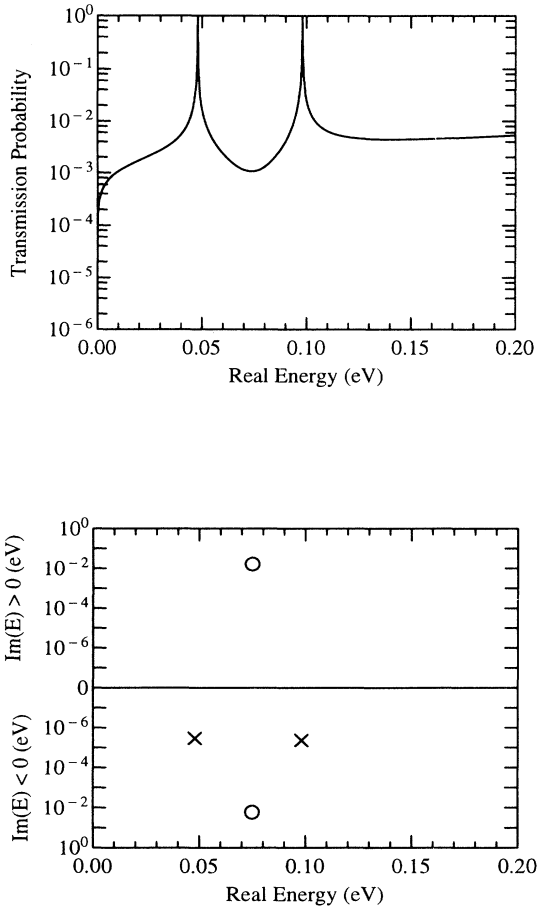

FIG. 9. (Top) Transmission coefficient vs incident electron energy for the analytic Fano resonance model (case 2). The matrix elements used are provided in Table III. In this case, the Fano resonances overlap and no transmission zeros exist between the resonances. (Bottom) Location of the poles (crosses) and zeros (circles) of $G^R(E)$ for this Hamiltonian. The zeros occur in complex conjugate pairs off of the real axis.

ishes at those locations. In Fig. 9, the difference between the bound state energies is only 0.050 eV and there is significant overlap between the resonances. In this case, the zeros have moved off of the real axis in conjugate pairs and the transmission probability does not vanish between the resonances. As the resonances are moved closer together, the two zeros approach each other on the real axis until the difference between the bound state energies is exactly 0.072 eV. For bound state energy differences less than 0.072 eV, the zeros move off of the real axis in conjugate pairs.

TABLE III. Matrix elements used in the analytic Fano resonance model for overlapped resonances and nonoverlapped resonances.

Matrix element	Isolated resonances	Overlapped resonances
w	1.0	1.0
t	0.05	0.05
V_1^L	0.03	0.03
V_1^R	0.03	0.03
V_2^L	-0.03	-0.03
V_2^R	0.03	0.03
B_1	0.05	0.05
B_2	0.15	0.10

This phenomenon may be understood qualitatively in terms of the amplitude and phase of the resonant and continuum channels. As mentioned previously, the resonant channel undergoes a phase shift of π as the incident energy passes through the pole. For an even parity bound state, the resonant channel is in phase with the continuum channel at energies below the pole and out of phase at energies above the pole. This implies that the amplitudes of the resonant channel and the continuum channel destructively interfere for energies greater than the pole energy. This explains the fact that the zero is located at a higher energy than the pole for the even parity resonance in Fig. 8. In this energy range, the amplitude of the resonant channel is decreasing (with increasing energy) while the amplitude of the continuum channel is increasing. The transmission zero occurs at the energy for which the amplitudes of the resonant and continuum channel are equal. However, if one adds a second resonant channel with a pole located at a slightly higher energy, the amplitude of the combined resonant channel may not decrease enough to equal the amplitude of the continuum channel. If this occurs, it is necessary to move off of the real energy axis in order for the amplitudes of the continuum and resonant channels to be equal. As the bound states are brought closer together in energy, this condition eventually occurs and the zeros move off of the real axis in conjugate pairs.

This is precisely what occurs in thicker AlAs barriers. As one increases the thickness of the AlAs barrier, the number of bound X states increases resulting in overlapping Fano resonances. Therefore, the zeros move off the real axis and the transmission probability no longer vanishes between resonances. In Fig. 5, there are two pairs of overlapping Fano resonances. In each case the real energy corresponding to the conjugate zeros is larger than either of the pole energies associated with the overlapped resonances. In our analytic model, this corresponds to the following condition:

$$|U_1| - |U_2| > B_2 - B_1 \ . \tag{29}$$

This simply indicates that the zero shift for the even parity state is larger than that for the odd parity state by an amount, which is greater than the difference between bound state energies.

As mentioned above, previous workers have explained the lack of transmission zeros by asserting that the conductivity through the continuum channel approaches zero.[2] We may investigate this scenario by letting t approach zero in our analytic model. In this limit, the numerator of the Green's function is no longer a function of energy (for bound states possessing opposite parity) and zeros no longer exist. However, as is shown in Fig. 5, this is not consistent with the locations of the poles and zeros of the Green's function for GaAs/AlAs/GaAs heterostructures.

VI. BAND-STRUCTURE EFFECTS ON FANO LINEWIDTHS

Further investigation of Fig. 5 reveals another interesting feature in the transmission curve. The spectral width of Fano resonances lying at energies above 0.19 eV is much larger than those lying below 0.19 eV. This phenomenon may be explained by examining the complex band structure of AlAs. In Fig. 10 the complex band structure of AlAs referenced from the Γ-valley minimum of GaAs is illustrated. The transition from narrow to broad Fano resonances corresponds to the X_1 energy (0.19 eV) labeled in Fig. 10. Below this energy, electrons in the AlAs barrier may occupy an evanescent Γ state and one of two propagating X-valley states with two different values of momentum. In the single-barrier structure, the propagating states are size quantized resulting in bound X states. The evanescent Γ states provide the continuum necessary for Fano resonances to occur. As illustrated in Fig. 7, the spectral width of a Fano resonance is determined by the overlap integral between the continuum evanescent state and the bound state. In this case, the continuum state possesses Γ-like symmetry while the bound state possesses X-like symmetry. The symmetry difference between these states implies a small overlap integral, which results in narrow resonance linewidths. The existence of two degenerate propagating (bound) states explains the split resonances lying below the X_1 energy in Figs. 2 and 5.

Above the X_1 energy, electrons may occupy an evanescent Γ state, a propagating X-valley state, and an evanescent state of X-like symmetry. Thus, at energies above the X_1 point (0.19 eV) there are in effect two sets of continuum evanescent states, one of which possesses Γ-like symmetry while the other possesses X-like symmetry. The significance of the evanescent X states on Fano resonances may be demonstrated by examining the wave function corresponding to a resonance energy lying above the X_1 point. In Fig. 11, the Bloch state amplitudes corresponding to the fifth resonance (energy = 0.217 eV) of the 34-Å AlAs barrier is plotted. This figure contains several interesting features. The amplitude of the evanescent X states (short dashed lines) is greater than unity and on the same order of magnitude as the amplitude of the propagating states. We can therefore conclude that the evanescent X states play an important role in determining the characteristics of this Fano resonance. Since the symmetry of these evanescent states is similar to the symmetry of the bound state, the overlap integral between these states is relatively large. The evanescent X states above the X_1 point act to significantly increase Fano resonance linewidths. This increase in linewidth implies that multiple resonances above this energy will overlap and the zeros of $G^R(E)$ will move off of the real axis. This explains the lack of transmission zeros above the X_1 point in the 34-Å barrier transmission curve. Additionally, we note that the right and left propagating X-valley states in Fig. 11 have different amplitudes. For a bound state (standing wave) these amplitudes would be equal. However, in this case, the interaction between the continuum and bound state results in an energy shift relative to the bound state energy.[13] This shift explains the difference between the left and right propagating state amplitudes.

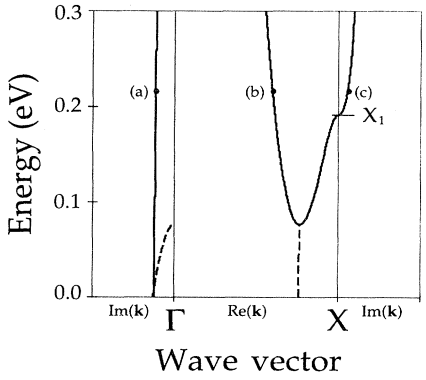

FIG. 10. Complex band structure of AlAs. Energy is referenced from the Γ-valley minimum of GaAs. Each quadrant of this plot is defined as follows. Left: $\mathrm{Re}(\mathbf{k})=0$, $\mathrm{Im}(\mathbf{k})\neq 0$. Center: $\mathrm{Re}(\mathbf{k})\neq 0$, $\mathrm{Im}(\mathbf{k})=0$. Right: $\mathrm{Re}(\mathbf{k})=\frac{2\pi}{a}$, $\mathrm{Im}(\mathbf{k})\neq 0$. Dashed lines indicate complex bands with $0<\mathrm{Re}(\mathbf{k})<\frac{2\pi}{a}$. (a) Evanescent Γ band. (b) Propagating X band. (c) Evanescent X band. The marked energy for these labels corresponds to the energy of the fifth resonance in the 34-Å AlAs barrier (0.217 eV). Complex bands emanating from bands lying far above the lowest conduction band have been omitted from this plot.

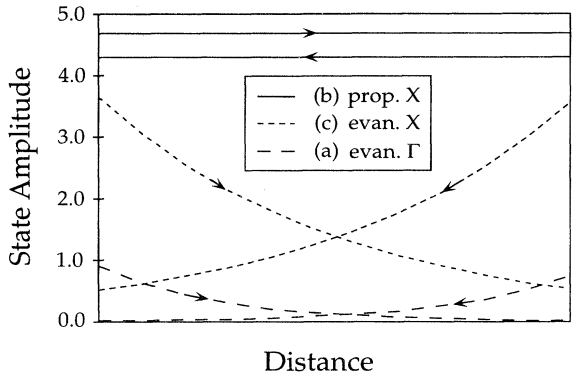

FIG. 11. Fano resonance wave function (energy = 0.217 eV) in the 34-Å AlAs barrier. The wave function is plotted in the bulk Bloch state representation. Solid line, propagating X-valley state. Short dashed line, evanescent X-state. Long dashed line, evanescent Γ state. The labels (a), (b), and (c) correspond to the complex band structure figure. The amplitude of the evanescent X state is above unity and contributes significantly to the continuum/bound state coupling, which determines Fano resonance linewidths. The difference in the amplitudes of the left and right traveling X-valley states is due to the Fano shift induced by this coupling.

VII. ANALYTIC LINE-SHAPE FITTING USING POLES AND ZEROS

The location of the poles and zeros of $G^R(E)$ characterize the transmission line shape in the vicinity of the

resonances and zeros.[15] Using the location of these poles and zeros, it is possible to generate accurate analytic fits for transmission line shapes. We assume that the transmission coefficient may be approximated as a rational function:

$$t(E) = \frac{\prod_i (E - E_i^z)}{\prod_j (E - E_j^p)} = \left[\prod_i (E - E_i^z)\right]\left[\sum_j \frac{R_j}{(E - E_j^p)}\right] , \quad (30)$$

where E^p and E^z represent the location of the poles and zeros of $G^R(E)$. The partial fraction expansion coefficients (R_j) are treated as fitting parameters for the transmission line shape. The real energy transmission amplitude is calculated at each pole location using Eq. (13). These values are then used to calculate a unique set of partial fraction expansion coefficients corresponding to the resonance line shape. A comparison between our analytic fit and the exact transmission line shape for the 34-Å AlAs barrier is shown in Fig. 12. We have included a transmission zero (E^z=0) at zero energy in the analytic expansion in order to force the condition $t(0) = 0$. As illustrated in Fig. 12, it is possible to obtain a rather accurate analytic fit to the transmission curve using only the locations of the poles and zeros of $G^R(E)$. Our analytic fit is most accurate in the vicinity of the resonances where one would expect the transmission amplitude to be a rational function. Numerically integrating the curves in Fig. 12, we find a relative error of only 4×10^{-3} between our analytic fit and the actual transmission curve. Since the majority of tunneling current in quantum devices flows through such resonances, it is clear that location of the poles and zeros of $G^R(E)$ may be employed to efficiently calculate tunneling current densities. We shall demonstrate the utility of our pole-zero locator in performing current density calculations in a later paper.

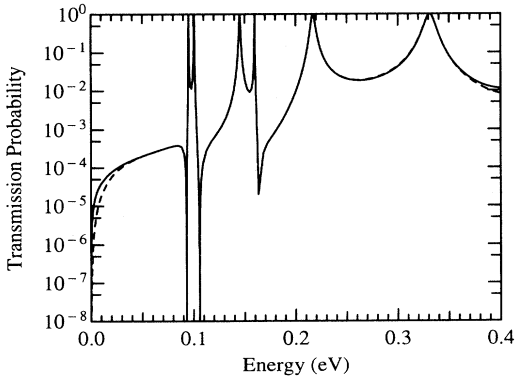

FIG. 12. Analytic fit of transmission probability curve for the 34-Å AlAs barrier. Solid line, actual transmission probability. Dashed line, analytic fit. In the vicinity of the resonances the analytic fitting function matches quite well. The largest deviations occur near energy = 0.0 eV and at energies lying between widely spaced resonances.

VIII. SUMMARY

The quantum transmitting boundary method has been generalized to provide open system boundary conditions for localized basis Hamiltonians. These boundary conditions allow one to calculate scattering states by simply solving a block-tridiagonal system of linear equations. A shift and invert nonsymmetric Lanczos algorithm has been developed to efficiently locate the poles and zeros of $G^R(E)$. These algorithms were applied to a single barrier AlAs heterostructure using the $sp3s^*$ tight-binding basis. We demonstrated that the location of the poles and zeros provides one with much insight into the phenomenon of Fano resonances in these structures. It was also shown that the transmission line shape near resonances can be fit analytically using the location of the poles and zeros of $G^R(E)$.

APPENDIX A: QTBM FOR SINGULAR COUPLING MATRICES

In the [100] direction, the $sp3s^*$ model results in Hamiltonian submatrices (D_j and S_j) of the following form:

$$D = \begin{bmatrix} A & V_{AC} \\ V_{CA} & C \end{bmatrix} , \quad (A1)$$

$$S = \begin{bmatrix} 0 & 0 \\ V'_{CA} & 0 \end{bmatrix} . \quad (A2)$$

The diagonal elements of D contain the on-site energy parameters for the zinc-blende anion (A) and cation (C) orbitals. The remaining submatrices (e.g., V_{AC}) contain the interatomic coupling parameters. Since the off-diagonal matrices S_j are singular, the formulation provided in Sec. II cannot be used for this model. This section details the formulation of the open system boundary conditions for this Hamiltonian.

The structure of S_j renders Eq. (4) invalid. To remedy this difficulty we employ a similar eigenvalue problem developed by Chang and Schulman.[16] However, the solution of this eigenvalue problem reveals that in the [100] direction, the $sp3s^*$ model contains only five (as opposed to ten) Bloch states traveling in each direction. Therefore, the matrices that provide the unitary transformation from the Bloch basis to the localized basis are singular,

$$\det \begin{vmatrix} \chi_1^R Z_1^{-1} & \chi_1^L Z_1 \\ \chi_1^R & \chi_1^L \end{vmatrix} = 0 , \quad (A3)$$

$$\det \begin{vmatrix} \chi_n^L Z_n^{-1} & \chi_n^R Z_n \\ \chi_n^L & \chi_n^R \end{vmatrix} = 0 . \quad (A4)$$

We therefore rewrite the unitary transformation given in Eqs. (7) and (8) as follows:

$$\begin{bmatrix} \Psi_0^A \\ \Psi_0^C \\ \Psi_1^A \\ \Psi_1^C \end{bmatrix} = \begin{bmatrix} \chi_1^{R_A} Z'^{-1}_1 & 0 & \chi_1^{L_A} Z'_1 & 0 \\ 0 & \chi_1^{R_C} Z'^{-1}_1 & 0 & \chi_1^{L_C} Z'_1 \\ \chi_1^{R_A} & 0 & \chi_1^{L_A} & 0 \\ 0 & \chi_1^{R_C} & 0 & \chi_1^{L_C} \end{bmatrix} \begin{bmatrix} a'_1 \\ a'_1 \\ b'_1 \\ b'_1 \end{bmatrix} , \tag{A5}$$

$$\begin{bmatrix} \Psi_{n+1}^A \\ \Psi_{n+1}^C \\ \Psi_n^A \\ \Psi_n^C \end{bmatrix} = \begin{bmatrix} \chi_n^{L_A} Z'^{-1}_n & 0 & \chi_n^{R_A} Z'_n & 0 \\ 0 & \chi_n^{L_C} Z'^{-1}_n & 0 & \chi_n^{R_C} Z'_1 \\ \chi_n^{L_A} & 0 & \chi_n^{R_A} & 0 \\ 0 & \chi_n^{L_C} & 0 & \chi_n^{R_C} \end{bmatrix} \begin{bmatrix} a'_n \\ a'_n \\ b'_n \\ b'_n \end{bmatrix} , \tag{A6}$$

where A and C label anion and cation, respectively. The subvectors and submatrices in these equations are of order 5. We may now express the incoming Bloch amplitudes in terms of the wave functions by computing the inverses of the matrices in (A5) and (A6):

$$\begin{bmatrix} \alpha'_1 & \beta'_1 \\ \gamma'_1 & \delta'_1 \end{bmatrix} = \begin{bmatrix} \chi_1^{R_A} Z'^{-1}_1 & 0 & \chi_1^{L_A} Z'_1 & 0 \\ 0 & \chi_1^{R_C} Z'^{-1}_1 & 0 & \chi_1^{L_C} Z'_1 \\ \chi_1^{R_A} & 0 & \chi_1^{L_A} & 0 \\ 0 & \chi_1^{R_C} & 0 & \chi_1^{L_C} \end{bmatrix}^{-1} , \tag{A7}$$

$$\begin{bmatrix} \alpha'_n & \beta'_n \\ \gamma'_n & \delta'_n \end{bmatrix} = \begin{bmatrix} \chi_n^{L_A} Z'^{-1}_n & 0 & \chi_n^{R_A} Z'_n & 0 \\ 0 & \chi_n^{L_C} Z'^{-1}_n & 0 & \chi_n^{R_C} Z'_n \\ \chi_n^{L_A} & 0 & \chi_n^{R_A} & 0 \\ 0 & \chi_n^{L_C} & 0 & \chi_1^{R_C} \end{bmatrix}^{-1} , \tag{A8}$$

$$a_1 = \begin{bmatrix} a'_1 \\ a'_1 \end{bmatrix} = \alpha'_1 \Psi_0 + \beta'_1 \Psi_1 , \tag{A9}$$

$$a_n = \begin{bmatrix} a'_n \\ a'_n \end{bmatrix} = \alpha'_n \Psi_{n+1} + \beta'_n \Psi_n . \tag{A10}$$

The QTBM operator is obtained by simply substituting Eqs. (11) and (12) with Eqs. (A9) and (A10).

APPENDIX B: GREEN'S FUNCTION DERIVATION OF OPEN SYSTEM BOUNDARY CONDITIONS

In this appendix we shall derive open system boundary conditions for multiband models in the Green's function formalism.[17] In this derivation the device Green's function is coupled to the semi-infinite leads using Dyson's equation. For the left boundary we obtain the following expression:

$$G^R_{11;ij} = g^R_{11;kl} + \sum_{kl} g^R_{11;ik}\, \Sigma^R_{L;kl}\, G^R_{11;lj} . \tag{B1}$$

Here, g^R corresponds to the retarded Green's function of the uncoupled system (device or lead), G^R corresponds to the Green's function of the coupled system, and Σ^R_L is a self-energy which arises due to the coupling of the spatially finite device to the left semi-infinite lead. The first pair of subscripts labels the spatial basis and the second pair of subscripts labels the tight-binding basis. The uncoupled device is defined over the spatial indices $[1, ..., n]$. The retarded Green's function for the open system is expressed in terms of the boundary self-energies as follows:

$$G^R = \begin{bmatrix} E - D_1 - \Sigma^R_L & S_2 & & & \\ S_2^\dagger & E - D_2 & S_3 & & \\ & \ddots & \ddots & \ddots & \\ & & S_{n-1}^\dagger & E - D_{n-1} & S_n \\ & & & S_n^\dagger & E - D_n - \Sigma^R_R \end{bmatrix}^{-1} . \tag{B2}$$

We therefore seek an expression for Σ_R^R and Σ_L^R. Employing Dyson's equation, the coupled Green's function G_{11}^R may be expressed as follows:

$$G_{11;ij}^R = g_{11;ij}^R + \sum_{kl} g_{11;ik}^R \, S_{1;kl}^\dagger \, G_{01;lj}^R \ , \tag{B3}$$

where

$$G_{01;ij}^R = \sum_{kl} g_{00;ik}^R \, S_{1;kl} \, G_{11;lj}^R \ . \tag{B4}$$

Combining Eqs. (B3) and (B4) we obtain the following form for G_{11}^R:

$$G_{11;ij}^R = g_{11;ij}^R + \sum_{klmn} g_{11;ik}^R \, S_{1;kl}^\dagger \, g_{00;lm}^R S_{1;mn} \, G_{11;nj}^R \ . \tag{B5}$$

Comparing Eqs. (B1) and (B5) we arrive at the following desirable form for Σ_L^R:

$$\Sigma_{L;ij}^R = \sum_{kl} S_{1;ik}^\dagger \, g_{00;kl}^R \, S_{1;lj} \ . \tag{B6}$$

Here, g_{00}^R corresponds to the Green's function at the boundary of the uncoupled semi-infinite lead.

In order to obtain g_{00}^R, we must write the equations of motion for the Green's functions g_{00}^R and g_{-10}^R in the uncoupled semi-infinite lead:

$$(IE - D_1) g_{00}^R + S_1^\dagger (\chi_1^R Z_1 \chi_1^{R^{-1}}) g_{00}^R = I \ , \tag{B7}$$

$$(IE - D_1) g_{-10}^R + S_1^\dagger (\chi_1^R Z_1 \chi_1^{R^{-1}}) g_{-10}^R + S_1 (\chi_1^R Z_1^{-1} \chi_1^{R^{-1}}) g_{-10}^R = 0. \tag{B8}$$

Note that in order to write these equations it is necessary to transform the Bloch propagation factors (Z_1 from Sec. II) into the tight-binding basis. Factoring out g_{-10}^R in Eq. (B8) and substituting into Eq. (B7) we obtain

$$- S_1 (\chi_1^R Z_1^{-1} \chi_1^{R^{-1}}) g_{00}^R = I \ . \tag{B9}$$

Rearranging terms, we may express the Green's function at the boundary of the right semi-infinite lead as follows:

$$g_{00}^R = -(\chi_1^R Z_1 \chi_1^{R^{-1}}) S_1^{-1} \ . \tag{B10}$$

Substitution of Eq. (B10) into Eq. (B6) results in an expression for the boundary self-energy in terms of the Bloch states in the leads and the coupling Hamiltonian,

$$\Sigma_{L;ij}^R = - \sum_k S_{1;ik}^\dagger \, (\chi_1^R Z_1 \chi_1^{R^{-1}})_{kj} \ . \tag{B11}$$

Note that the Green's function [Eq. (B2)] generated from this boundary self-energy is in the tight-binding representation. Therefore, each column of G^R represents the response of the system due to a particle which has been injected in a tight-binding basis state. This is in direct contrast to the Green's function resulting from the QTBM formulation. The first and last N (N is the number of basis states) columns of the QTBM Green's function correspond to the response of the system due to injection from Bloch states in the leads. Thus, with the QTBM formalism one may obtain all of the relevant transport information by generating only the columns of G^R corresponding to propagating states. In the Green's function formalism it is necessary to generate N columns of the Green's function to calculate the observables necessary for transport.

[1] J. Schulman and Y. C. Chang, Phys. Rev. B **31**, 2056 (1985).
[2] D. Y. K. Ko and J. C. Inkson, Semicond. Sci. Technol. **3**, 791 (1988).
[3] P. Roblin, Superlatt. Microstruct. **4**, 363 (1988).
[4] D. Z.-Y. Ting, E. T. Yu, and T. C. McGill, Phys. Rev. B **45**, 3583 (1992).
[5] T. B. Boykin and J. S. Harris, Jr., J. Appl. Phys. **72**, 988 (1992).
[6] C. S. Lent and D. J. Kirkner, J. Appl. Phys. **67**, 6353 (1990)
[7] J. H. Wilkinson, *The Algebraic Eigenvalue Problem* (Clarendon Press, Oxford, 1965), pp. 388–405.
[8] G. H. Golub and C. F. Van Loan, *Matrix Computations* (Johns Hopkins University Press, Baltimore, 1989), Chap. 9.
[9] T. Ericsson and A. Ruhe, Math. Comp. **35**, 1251 (1980).
[10] C. Fernando and W. R. Frensley, J. Appl. Phys. **76**, 2881 (1994).
[11] K. V. Rousseau, K. L. Wang, and J. N. Schulman, Appl. Phys. Lett. **54**, 1342 (1989).
[12] R. Beresford, L. F. Luo, W. I. Wang, and E. E. Mendez, Appl. Phys. Lett. **55**, 1555 (1989).
[13] U. Fano, Phys. Rev. **124**, 1866 (1961).
[14] P. Vogl, H. P. Hjalmarson, and J. D. Dow, J. Phys. Chem. Solids **44**, 365 (1983).
[15] Z. Shao, W. Porod, and C. S. Lent, Phys. Rev. B **49**, 7453 (1994).
[16] Y. C. Chang and J. N. Schulman, Phys. Rev. B **25**, 3975 (1982).
[17] J. A. Støvneng and P. Lipavský, Phys. Rev. B **49**, 16 494 (1994).